ADVANCED BIOSYSTEMS
www.adv-biosys.com

Carcinomas with Occult Metastasis Potential: Diagnosis/Prognosis Accuracy Improvement by Means of Force Spectroscopy

Anahid Amiri, Florian D. Hastert, and Christian Dietz**

Accurate diagnosis of cancer stage is inevitable for the following prognosis in patients struggling with these lesions to promote their health and survival rate. Previous studies on survival rate statistics show, in some cases, failure in cancer stage surveys in which metastasis or recurrence of the disease was not accurately prognosed. Morphology study of cancer cells advances the understanding about cancer behavior and its progression, in which, in our previous study on invasive cancer cells, fewer formations of cytoskeleton components compared to their counterparts was observed. Here it is shown that carcinomas with an occult propensity of metastasis depict a number of poorly differentiated cells with decreased amounts of cytoskeleton components in a near-well differentiated population. Force spectroscopy in conjunction with fluorescence microscopy of lung cancer, liver hepatoma, and melanoma provides a general view of these cells' architecture, leading to the conclusion that the scarce abnormal-shaped cells with low formation of structural filaments convey the high risk of metastatic potential of the tumor. The results demonstrate that force spectroscopy complements conventional diagnostic approaches by an accurate cytoskeleton assessment and can improve the following prognosis in epithelial cancers with occult metastasis risk.

1. Introduction

Recent studies on survival rate statistics show in some cases failure in cancer stage surveys in which metastasis or recurrence of the disease was not accurately prognosed.[1–4] Unraveling the morphology of cancer cells in comparison to their normal counterparts is a significant step toward understanding cancerous behavior. In our previous study,[5] we investigated structural and physical properties alteration of mammary cells due to the transition from a healthy state to carcinoma. We could not justify the softening of invasive ductal carcinoma (IDCs) compared to healthy counterparts based on epithelial–mesenchymal transition as the IDCs we investigated were from a nonmotile ductal carcinoma without a phenotypic shift. However, based on atomic force microscopy measurements decreased formation of microtubules in cancerous cells compared to their counterparts was found to be the most likely cause for the overall change in mechanical properties. This motivated us to look into other invasive carcinomas, which are among the most diagnosed fatal cancers, to get a better understanding on epithelial cancerous cells architecture and behavior in malignancy and metastasis stages. This was further driven by studies, which have shown that the conventional cancer classification approach is insufficient for tumors with a biological propensity to metastasize when, for example, a majority of patients who eventually develop metastatic disease and die of melanoma are initially diagnosed as stage I or II.[1] In recent years, efforts have been done to use force microscopy in vitro as a new diagnostic approach for detecting metastatic cells.[6–9] The goal of this study is to provide a more general image of carcinoma cells with occult metastasis and to improve the accuracy of diagnostic approaches based on cytoskeleton assessment that makes force microscopy indispensable for this purpose due to its ability to mechanically sense polymerized cytoskeletal components and to distinguish them from the unpolymerized counterparts. Improving the diagnosis could further refine the following prognosis and treatment procedure efficacy in patients struggling with occult metastatic potential lesions. For this aim, we have chosen three invasive carcinomas HS695T melanoma cells, Calu_1 lung cancer and PLC/PRF/5 liver hepatoma for our research.

The HS695T metastatic amelanotic melanoma cell line was isolated from lymph nodes. In its initial assessments, the HS695T cell line shows a doubling time of ≈48 h, moderate saturation density, moderate grow in semisolid media and colony formation. They consisted mostly of stellate- and

A. Amiri, Dr. C. Dietz
Physics of Surfaces, Department of Materials Science
Technische Universität Darmstadt
Alarich-Weiss-Str. 2, Darmstadt 64287, Germany
E-mail: amiri@pos.tu-darmstadt.de; dietz@pos.tu-darmstadt.de
Dr. F. D. Hastert[+]
Cell Biology and Epigenetics, Department of Biology
Technische Universität Darmstadt
Schnittspahnstraße 10, Darmstadt 64287, Germany
The ORCID identification number(s) for the author(s) of this article can be found under https://doi.org/10.1002/adbi.202000042.
[+]Present address: Max Planck-Bristol Centre for Minimal Biology, Cantock's Close, Bristol BS8 1TS, UK

DOI: 10.1002/adbi.202000042

polygonal-shaped cells with enlarged prominent nuclei. Furthermore, inoculation of HS695T did not produce tumors.[10] We have chosen the HS695T cell line due to its moderate pathological behavior whereas it was metastasized to nodes, as a sample with mid-grade tumor characteristics and a high risk of circulation. Non-small-cell lung cancer (NSCLC) accounts for 85%–90% of all lung cancers.[11] Although small cell lung cancer is considered the more aggressive cancer with a faster doubling time, higher growth fraction, and more rapid development of metastasis,[12] drug resistance in NSCLCs with a more moderate clinical behavior is the main reason of therapeutic collapses and disease deterioration.[13] We selected squamous cell lung carcinoma cells Calu_1 isolated from metastatic pleural space as a representative of NSCLCs with metastasis potential. Liver cancer is the fourth leading cause of global cancer mortality, with ≈90% of these lesions being hepatocellular carcinomas developing mainly in patients with chronic liver disease which established cirrhosis as a result of viral hepatitis (B or C) infection, alcohol abuse, and nonalcoholic fatty liver disease.[14,15] Furthermore, the liver is the major metastasis destination of many cancers[14] due to its hospitable biological condition. We investigated PLC/PRF/5 hepatocellular cell line (Alexander cells) considering its characteristics as approved representative of primary liver cancer cell lines in vitro with poor prognosis and occult metastases.[14]

We do not cancel out the doubt in alteration of cells properties and characteristics as well as genomic signatures of cells derived from cell lines due to successive culturing compared to primary cells derived from mouse model or patient's lesion. Nevertheless, we were confident to design our preliminary experiment based on cell lines with due attention to their easy handling and longer periods of time in culture, considering previous studies on assessing the changes imposed to cell lines compared to the primary cells. These studies reveal that most cell lines are trusted to be representative of morphological features[16] and although they are in culture for many years or decades they have not accumulated substantial new recurrent aberrations during extended culture and mirror the genomic signature of primary cells.[17–20] References [18–20] support the collecting of the three metastatic cell lines (breast ductal carcinoma, NSCLC, and hepatocellular carcinoma) as authentic cell lines for cancer research. Given that the comparison of healthy and cancerous ductal carcinoma revealed an immense difference in cytoskeleton formation among these two cell lines in concert with fluorescence images that show normal polymerization and levels of cytoproteins for the healthy cell line,[5] we can further affirm the physiological relevance of healthy and diseased cells based on cell line surveys.

2. Results and Discussion

2.1. Cutaneous Melanoma

A majority of patients who eventually develop metastatic cancers and die of melanoma are initially diagnosed as stage I or II, which indicates the tumors with a biologic propensity to metastasize that are currently not being identified.[1–4] Although sentinel lymph node biopsy (SLNB) remains an important prognostic tool in patients with melanoma, findings from the Multicenter Selective Lymphadenectomy Trial-1 study indicate that two out of three patients who died of melanoma were SLN negative.[1] These statistics show a high percentage of error in diagnosis and the following prognosis based on traditional tumor grading and underline that the conventional cancer classification approach is insufficient. Many recent studies on molecular cancer characterization and gene expression profiling have shown a more accurate tumor classification outcome,[21–25] as the 31-gene expression profile (31-GEP) test for cutaneous melanoma (CM) identifies accurately and independently high-risk tumors within low-risk populations, including node negative, stage I-IIA and T1 (<1 mm) CM.[1] On the other hand, advanced image analysis is also producing new insights, providing quantitative confirmation of many existing diagnostic criteria. Atomic force microscopy provides images based on mechanical properties of cells on each pixel volume that gives a 3D information of cells. This characteristic puts AFM as a competitor among other imaging methods to be an outstanding characterization tool in cell studies.

We imaged melanoma cells at their fourth and sixth passage of culture in our lab with a very low setpoint of 50 pN (shown in **Figure 1**) to have the least disturbance on the cell structure. In our images, combinations of the three morphologic types of often bipolar shape that is the normal shape of melanocytes,[26] and some cases of stellate and polygonal cell shapes can be seen. Cells mostly indicate actin filaments structure and dense formation of cell–cell junctions. Imaging clusters of parallel structures of fine actin filaments to the cell membrane was attainable based on the lateral resolution of images (≈44 nm with a very small tip radius size of 10 nm) shown in Figure 1 and a low set point with shallow indentation. Yet, in Figure 1a,b round shaped cells with distorted formation of architectural filaments can be seen. These cells show round enlarged nuclei compared to their bipolar-shaped peer cells.

We also imaged melanoma cells at the 14th passage of culture with a high set point force of 2 nN. At this point, we chose a single noncontacted polygonal shape cell to be imaged. Images are shown in **Figure 2**. We observed a dense structure of filaments on the long axis of the cell, yet, in distorted angular region (pointed in Figure 2 error image), an ordered formation of architectural filaments was not detectable. The super high-resolution imaging (≈22 nm per pixel) allows us to see the distribution of stiffness on the cell and studying the mechanical properties of important cellular organelles as for example the rough endoplasmic reticulum (RER) in the halo adjacent to the nucleus (pointed in Figure 2 deformation image). The height, deformation, and elastic modulus distributions on the cell are shown in **Figure 3**. The values are derived from the line drawn on the elastic modulus image in Figure 2. The profile of the apparent height shows a maximum at the nucleus region compared to the cellular periphery of the cell whereas depicting the lowest stiffness value of ≈110 kPa with high deformability of ≈270 nm. Adjacent to the nucleus an elevation can be seen in the height profile with a correlating high stiffness value compared to the nucleus of ≈570 kPa and low deformability of ≈100 nm, presumably showing the ER organelle.

Although, comparison of the configuration of the melanoma cells to one another on AFM images shows some poorly differentiated cells that are depicting significantly

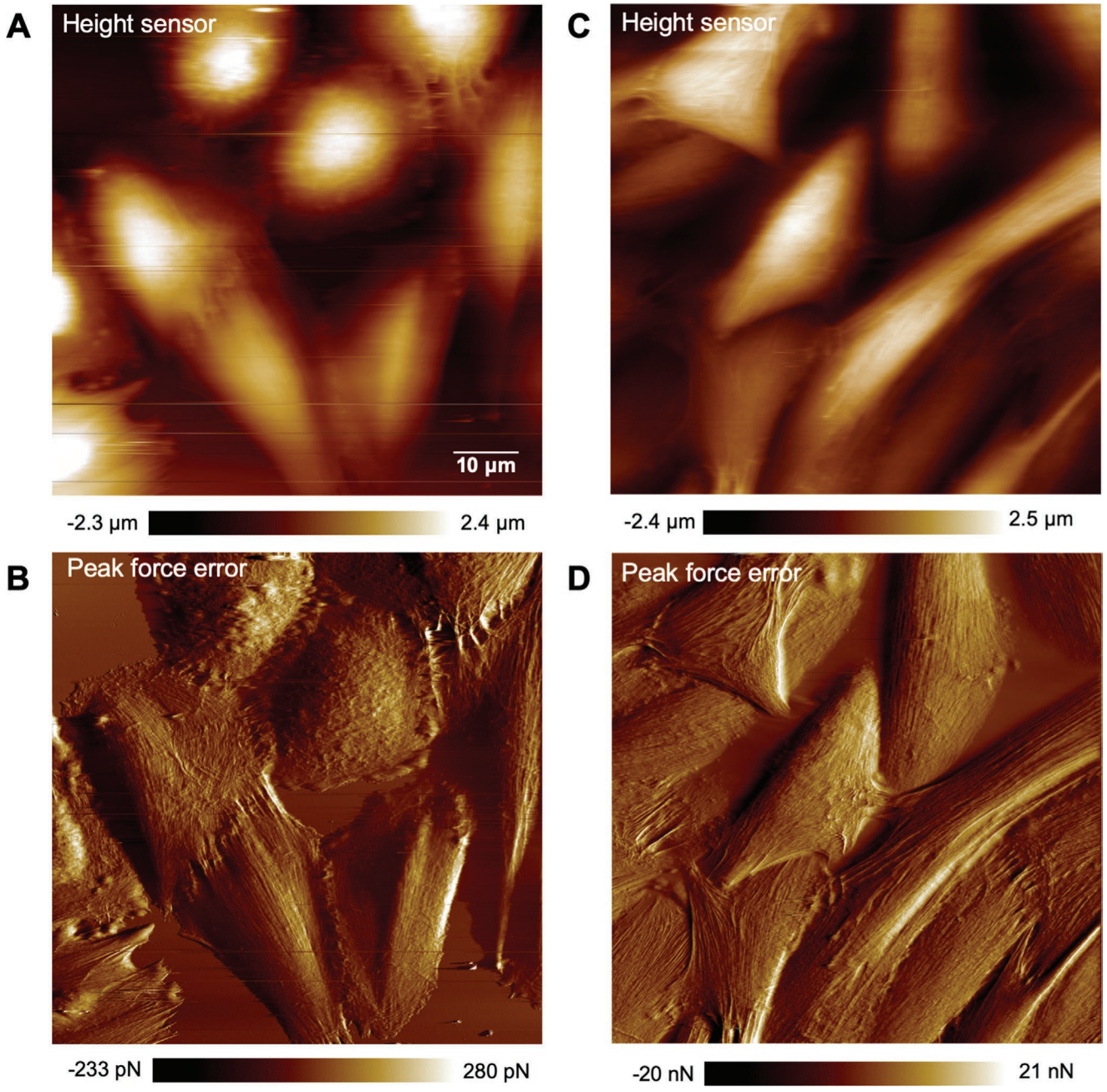

Figure 1. High resolution (2048 pixels × 2048 pixels/≈44 nm per pixel) topography, force error maps of amelanotic melanoma cells at A,B) fourth passage of our culturing process and C,D) at sixth passage of culture, 24 h after seeding them on plasma treated coverslips measured in the CO_2-independent growth medium by PFT-AFM. A,C) topography images and B,D) peak force error images using a setpoint force of 50 pN, an oscillation amplitude of 300 nm and a driving frequency of 0.25 kHz for imaging the cells.

lower formation of structural filaments, AFM images in concert with fluorescence microscopy images of HS695T cells (shown in Figure 8a) show mostly near-normal formation of filaments with bipolar shaped cell that characteristically could be misinterpreted in conventional cancer classification approach as a low-grade tumor. The above-mentioned statistics and analyzing the HS695T cells taken as mid-grade tumor cells with high risk of metastasis, combined with our previous study that shows the highly metastatic invasive ductal carcinomas with relative lack of cytoskeletal components formation compared to its healthy counterparts,[5] we hypothesize that the scarce abnormal-shaped cells with low formation of structural filaments in the majority of near-normal bipolar-shaped cells population bear the high risk of metastatic potential of the tumor.

Adhesion of cells in vitro on the glass coverslip is mediated by adhesion proteins like vitronectin and fibronectin, which are contained in serum-supplemented culture medium.[27]

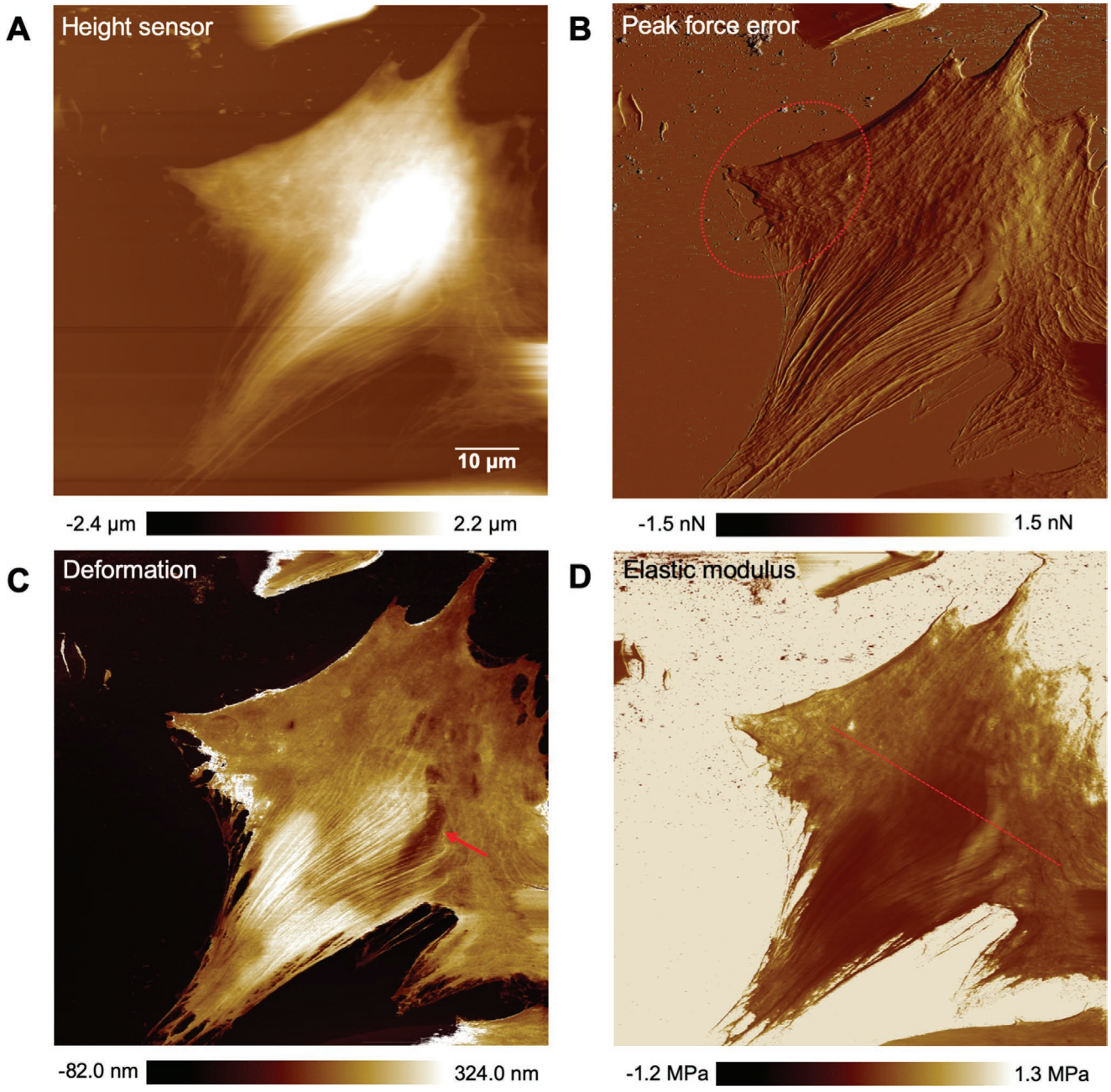

Figure 2. Super high-resolution (≈22 nm per pixel) topography, force error and deformation and elastic modulus maps of amelanotic melanoma cells. A) topography, B) peak force error, C) deformation and D) elastic modulus using a setpoint force of 2 nN, an oscillation amplitude of 300 nm and a driving frequency of 0.25 kHz for imaging the cells.

In this respect, the HS695T cell line shows no fibroblast-like morphology in the later passages of initial culturing,[10] for the sake of better cell adhesion, it is known to use FBS-containing cell culturing media. Vitronectin is present at a far higher concentration than fibronectin in FBS[27] and we assume the surface of the negatively charged plasma treated glass coverslip is initially covered by the vitronectin proteins to ease the cell adhesion. Vitronectin contains an RGD motif consisting of positively charged amino acids at pH 7, which provides a cationic charged surface and in turn attaches to the integrin bound to the focal adhesion of the cells. In our images shown in **Figure 4**, the complex of intracellular face of the membrane at focal adhesion regions shows highly negative charges based on significant adhesion between the lining of the cells and the silicon nitride cantilever tip that gets positively charged at a pH lower than 8.[28] We exclude the major influence of the substrate charges in the region of focal adhesion due to the apparent height of ≈200 nm and surface charge neutralization by adhesion-promoting extracellular matrix proteins. On the other hand, single fine cell filaments can be distinguished

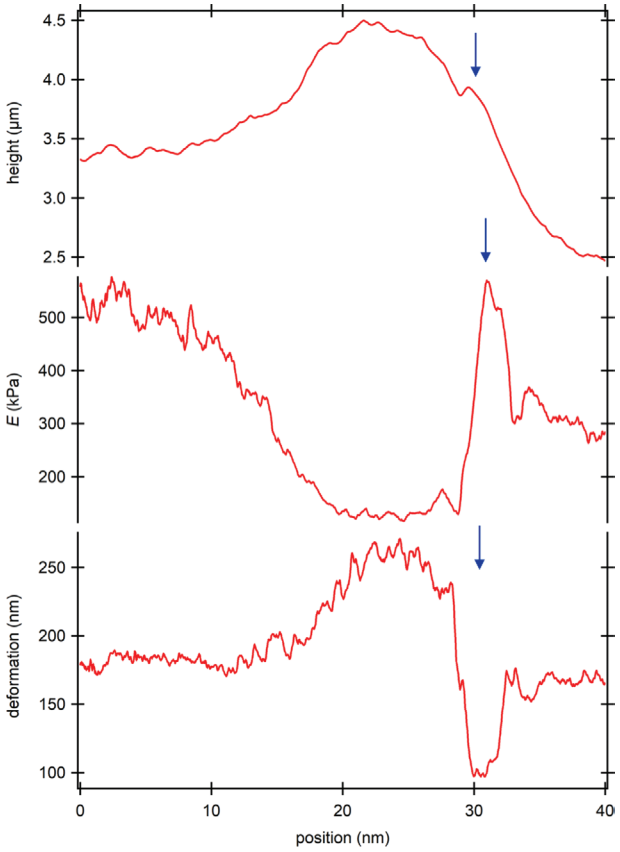

Figure 3. Height, elastic modulus and deformation distribution on cell derived from the line marked on the elastic modulus image in Figure 2. The arrows show the ER height, elastic modulus and deformation values.

separately as it is observable in Figure 4d. These fine details on cell structure could be attained by super high-resolution imaging that is of high interest for the cell biophysics community.

2.2. Non-Small-Cell Lung Cancer

Heat shock protein 27 (HSP27) is an antiapoptotic agent and has been characterized with the ability to regulate actin cytoskeletal dynamics during heat shock and other stress conditions, functioning both to promote actin polymerization and as an actin capping protein.[29] HSP27 can directly inhibit actin polymerization by capping the barbed end of F-actin[30–32] and by sequestering globular actin (G-actin).[32,33] Studies on protein expression levels in cancer cells indicated the overexpression of HSP27 to be potentially involved in the aggressiveness of NSCLCs.[34] Furthermore, overexpression of HSP27 is reported to be the reason of poor prognosis and drug resistance in NSCLCs.[34,35] On the other hand, recent studies on cytoskeleton components show the three actin filaments, intermediate filaments, and microtubules to have an extensive crosstalk with one another in different biological processes. Specifically, the two cytoskeletal systems F-actin and microtubules often work together in core cellular processes and that their functional dynamic properties are often intimately intertwined as actin-microtubulin mediated growth or actin-mediated anchoring and stabilization of microtubule ends.[36] This implies that dysregulated F-actin can cause further distortion in the cytoskeleton configuration.

AFM images on Calu_1 cell line indicate poorly differentiated and mostly polygonal-shaped cells (shown in **Figure 5**a topography and Figure 5b peak force error at low force $F = 200$ pN; Figure 5c topography and Figure 5d adhesion image at high force $F = 2$ nN). Cytoskeleton components on polygonal-shaped cells are totally distorted and not fully formed to protect the nuclei or to support the shape of the cells. This observation in AFM images of Calu_1 is in line with the results from fluorescence microscopy images (shown in Figure 8b). The increased expression of HSP27 in poorly differentiated NSCLC tissues compared to moderately and well differentiated NSCLC tissues[34] and considering its interaction with the F-actin cytoskeleton could highly justify cell morphological abnormality in these types of lesions.

2.3. Hepatocellular Carcinoma

High-resolution AFM images (shown in **Figure 6**a topography and Figure 6b peak force error at low force $F = 200$ pN; Figure 6c topography and Figure 6d adhesion image at high force $F = 2$ nN) in concert with fluorescence microscopy images (shown in Figure 8c) on Alexander cells show significantly poor formation of supportive dynamic cytoskeleton components and lesser defined shape of cells compared to the two other investigated cell lines in this study. Cells mostly depict round configuration with scarce cytoplasm and prominent enlarged nuclei taking the vast majority of the cell portion. Additionally, AFM images on liver carcinoma cells depict pronounced borders visible as a bold rim in the region of connection to the neighboring cells. Cross-checking with fluorescence images, the borders show concentration of actin in the region of stress fibers (shown in Figure 8c), hence justifies the pronounced appearance of the borders in the AFM images.

As depicted in **Figure 7** it is reasonable to believe that the dominant group of filaments formed on the cells is intermediate filaments due to their coiled-coil structure displayed in Figure 7b.

Visual comparison of cytoskeleton formation based on fluorescence images (shown in **Figure 8**) reveals HS695T cells with relatively normal formation of both dynamic cytoskeleton components, Calu_1 cells with highly distorted F-actin and a few polymerized tubulins that are most obvious in the cell with the largest size in Figure 8b and PLC/PRF/5 cells with mainly lack of both dynamic filaments on the main body of the cell whereas actin filaments are still observed on the borders of the cells. These results are completely in line with the AFM images.

Nevertheless, pancellular levels of F-actin labeled with TRITC-conjugated phalloidin (**Figure 9**a) and pancellular levels of β-tubulin labeled with an AF-488 labeled antibody (Figure 9b) which were quantified by widefield high-content

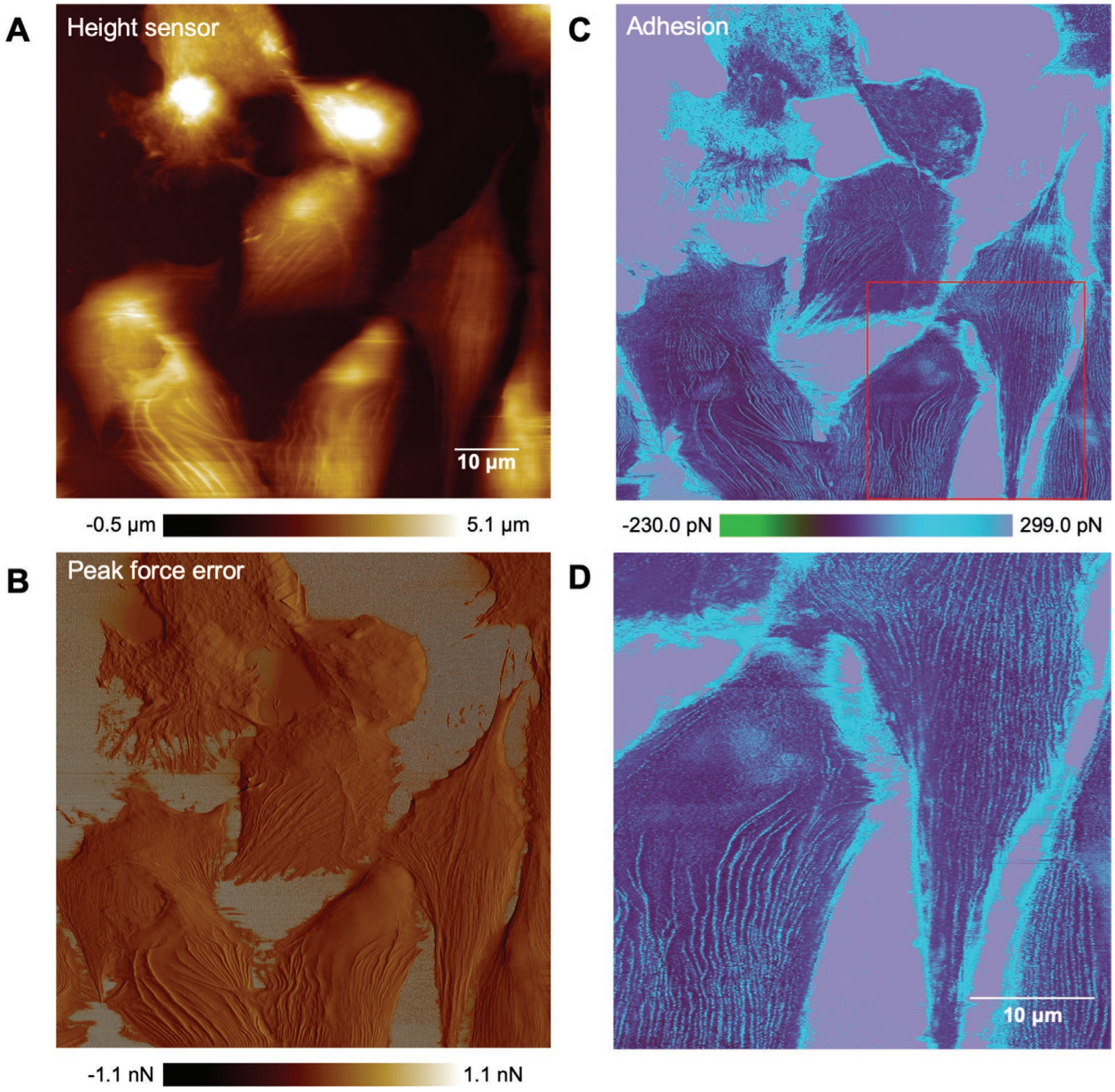

Figure 4. Super high-resolution (4096 pixels × 4096 pixels/≈22 nm per pixel) topography, force error, and adhesion maps of amelanotic melanoma cells. A) Topography, B) peak force error, C) adhesion, and D) enlarged image of the framed area in adhesion image using a setpoint force of 50 pN, an oscillation amplitude of 300 nm and a driving frequency of 0.25 kHz for imaging the cells.

screening microscopy show higher intensity levels of β-tubulin and actin in Calu_1, PLC/PRF/5 and BT20 with highly distorted cytoskeleton, in comparison to HS695T cells. Note that invasive ductal carcinoma BT20 cell line was investigated in our previous study.[5] To demonstrate the correlation between the levels of cytoskeleton-proteins and cells' physical properties, we correlate the stiffness values (assessed comprehensively in Amiri et al.[5]) to the integrated pancellular levels of tubulin and actin in **Table 1**. BT20, Calu_1 and PLC/PRF/5 cells, as aforementioned with a fair bit loss of cytoskeleton components, show lower stiffness values (refer to Table 1) with higher levels of subunits compared to HS695T cells (refer to Figure 9) with an average stiffness value of 150 kPa. These results can be explained by a significant cytoskeleton instability in malignant cancer cells despite a sufficient filament subunit level.

For further support of the presented results, we provide deformation values on each cell line that affirms the better polymerization and structural integrity of HS695T cell line which is less invasive in comparison to the other three studied cell lines with metastatic potential. Table 1 shows the deformation of Calu_1 and BT20 cells with the highest peak values of 260 and 258 nm, respectively, followed by PLC/PRF/5 with 185 nm and HS695T with 150 nm, read out from the histogram

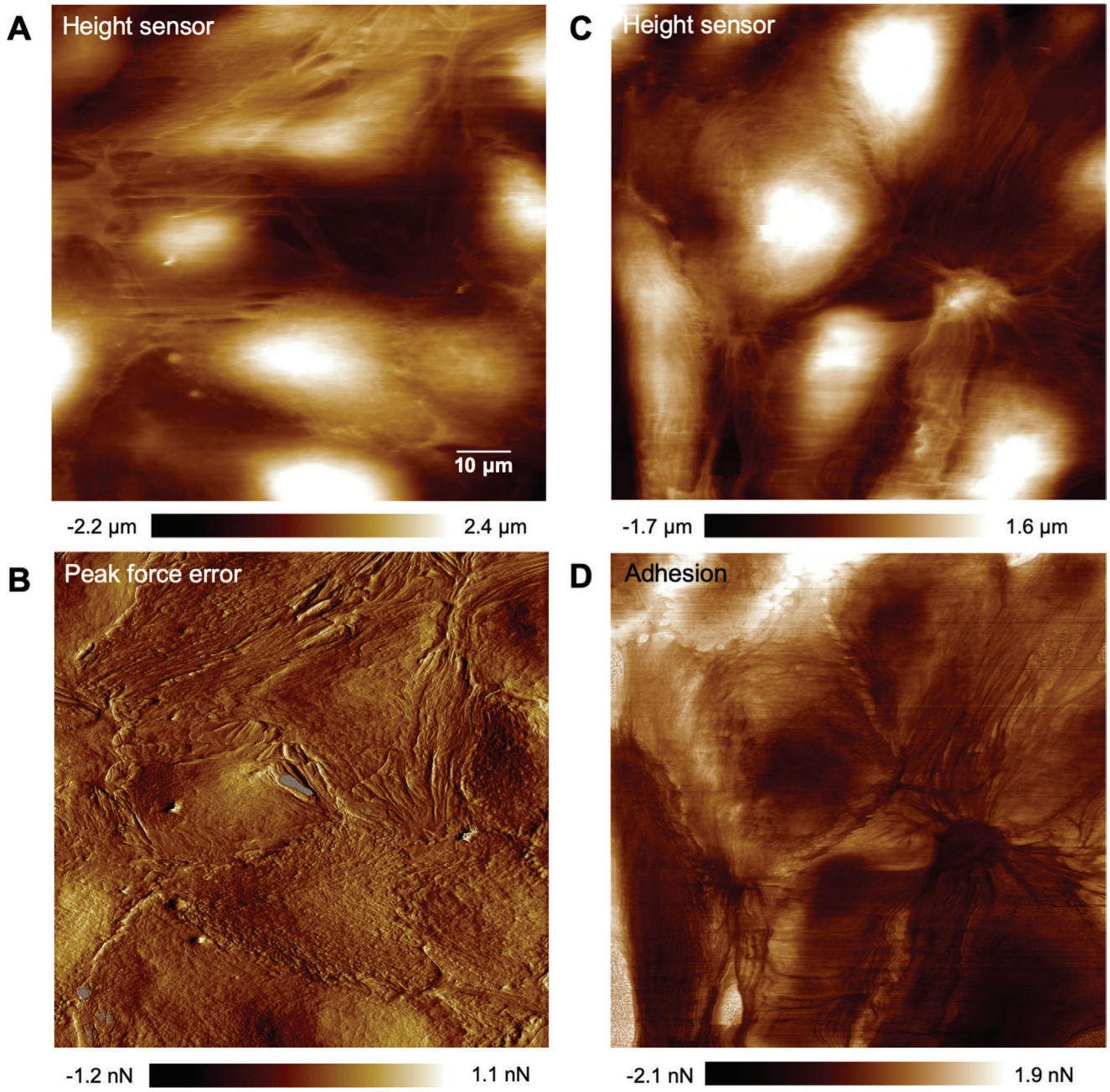

Figure 5. High resolution (2048 pixels × 2048 pixels/≈44 nm per pixel) maps of NSCLC on two samples of low passages A,B) fourth and C,D) fifth of culture, 24 h after seeding them on plasma treated coverslips measured in the CO_2-independent growth medium by PFT-AFM. A) Topography image and B) peak force error image using a setpoint force of 200 pN, C) topography image and D) adhesion image using a setpoint force of 2 nN, an oscillation amplitude of 300 nm and a driving frequency of 0.25 kHz for imaging the cells.

(Figure S1, Supporting Information, density of deformation values).

3. Conclusion

According to our observations and structural analysis of the epithelial cancer cell lines with high-risk metastasis by means of AFM in concert with fluorescence microscopy, we postulate distortion in formation of filaments is showing the malignancy of the cells and is the reason for observing a variety of shapes among cancerous cells, and specifically showing the metastatic potential of the tumor. We stress that the cell lines Calu_1, PLC/PRF/5 and BT20 (used in the previous study) were all invasive epithelial cell lines originally derived from metastatic sites in the patient's body and used as representatives of high stage cancer to be analyzed. Although HS695T was invasive

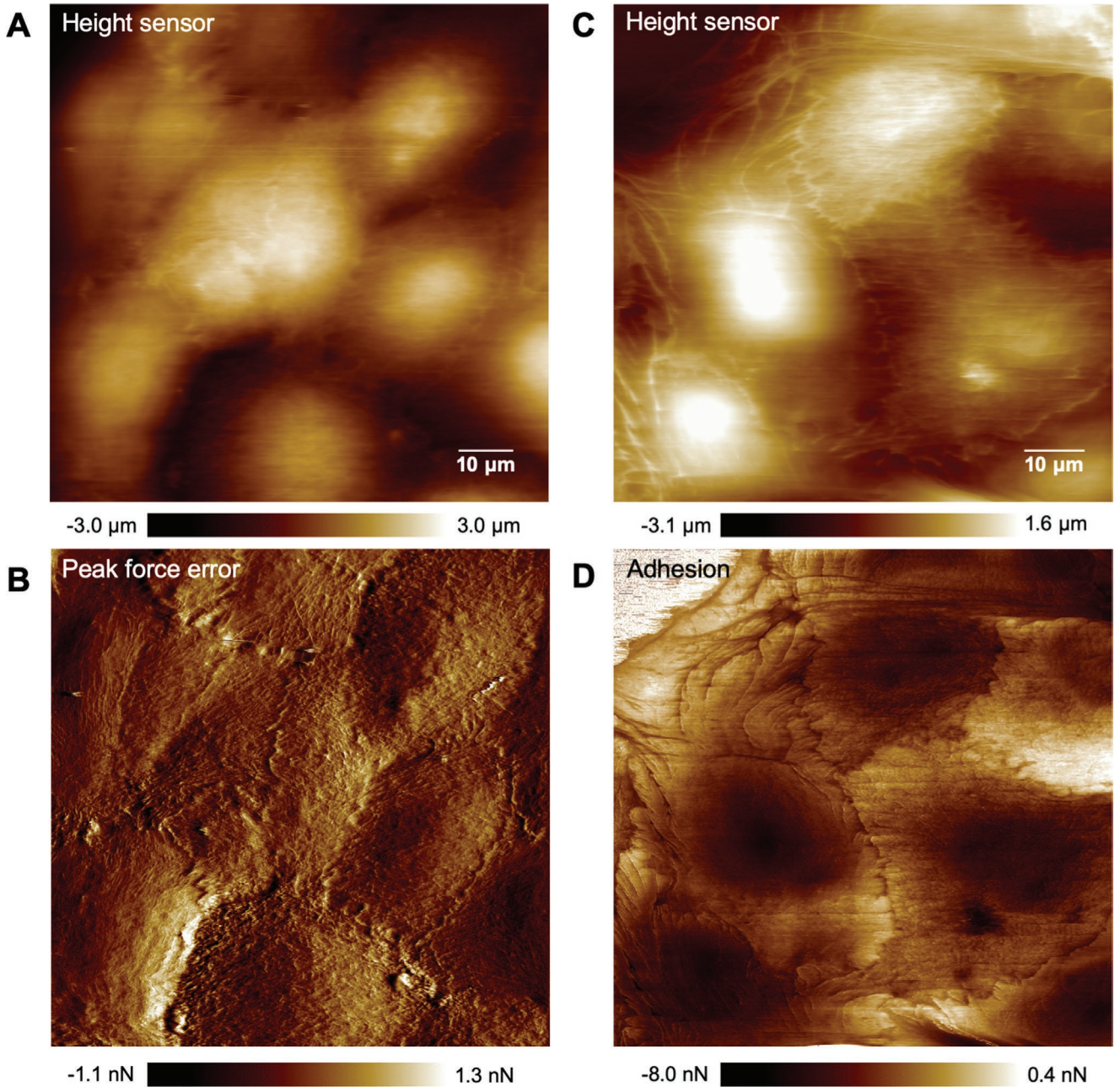

Figure 6. High resolution (2048 pixels × 2048 pixels/≈44 nm per pixel) maps of Alexander cells at fourth passage of culture, 24 h after seeding them on plasma treated coverslips measured in the CO_2-independent growth medium by PFT-AFM. A) Topography image and B) peak force error image using a setpoint force of 200 pN, C) topography image and D) adhesion image using a setpoint force of 2 nN, an oscillation amplitude of 300 nm and a driving frequency of 0.25 kHz for imaging the cells.

and derived from lymph nodes, in later assessments it showed moderate pathological behavior and no tumor production after animal inoculation.[10] According to Gastman et al.,[1] the conventional cancer classification approach is insufficient for tumors with a biological propensity to metastasize when, for example, a majority of patients who eventually develop metastatic disease and die of melanoma are initially diagnosed as stage I or II. We chose HS695T amelanotic melanoma with considering its pathological behavior, as carcinoma with occult metastasis model for our preliminary experiment. Given that the diagnosis of tumors with high risk of metastasis by specific protein expression tests depends on the cell type and is still not suitable for all cancer types and can furthermore differ from individual to individual, seeking a general diagnostic approach with high accuracy is vital.

Due to acquisition of images based on mechanical properties, atomic force microscopy can sense polymerized cytoskeleton components as continuous and rigid elements

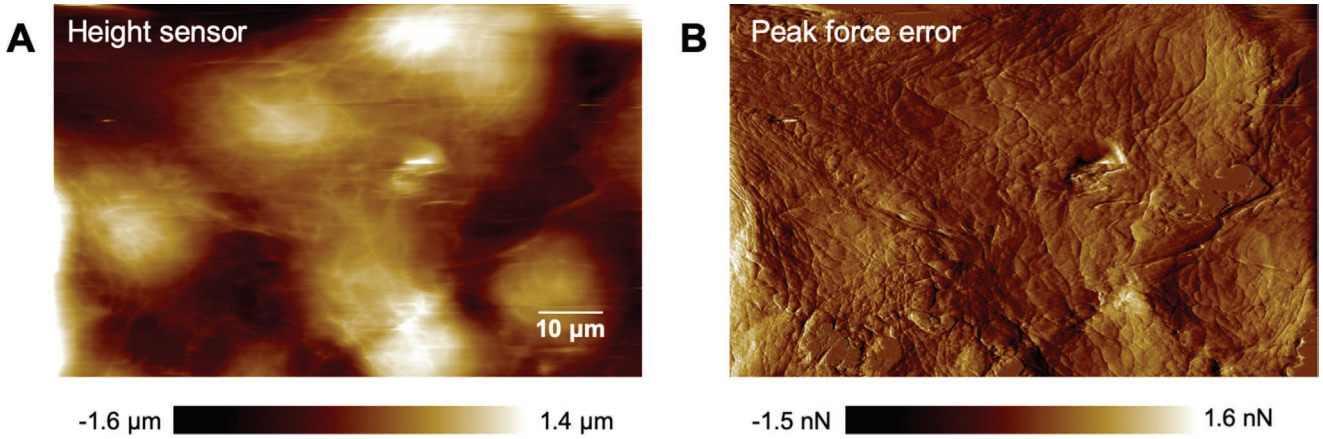

Figure 7. High-resolution (≈44 nm per pixel) maps of Alexander cells at 4th passage of culture, 24 h after seeding them on plasma treated coverslips measured in the CO_2-independent growth medium by PFT-AFM. A) Topography image and B) peak force error image using a setpoint force of 2 nN, an oscillation amplitude of 300 nm and a driving frequency of 0.25 kHz for imaging the cells.

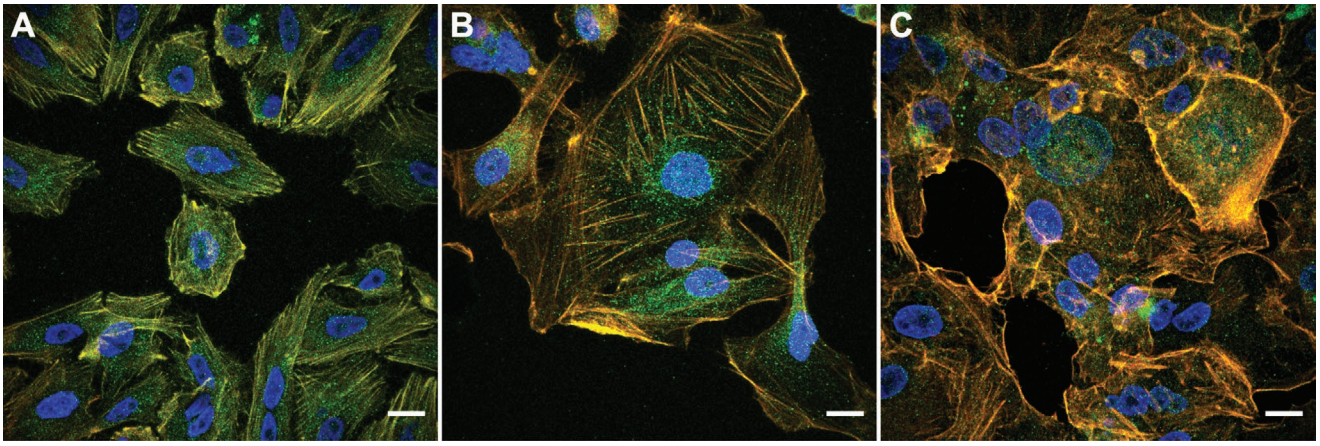

Figure 8. Representative confocal fluorescence microscopy images. A) HS695T cell line, B) Calu_1 cell line and C) PLC/PRF/5 cell line which were stained with TRITC-conjugated phalloidin against F-actin and an AF-488-conjugated monoclonal antibody against β-tubulin and counterstained with DAPI. Scale bars = 10 µm.

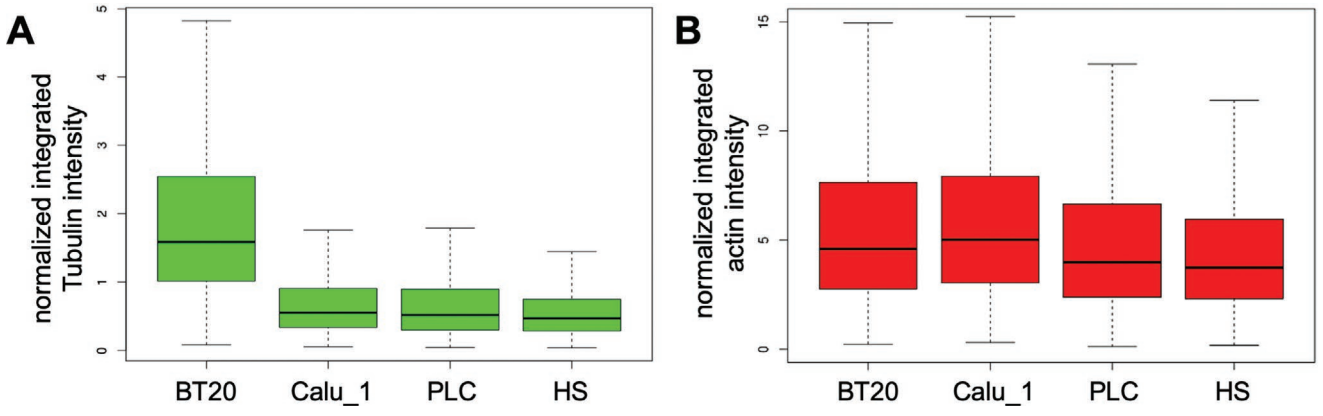

Figure 9. Integrated pancellular levels. A) β-tubulin labeled with AF-488-conjugated monoclonal antibody and B) F-actin labeled with TRITC-conjugated phalloidin. Respective fluorescence intensity levels were quantified by widefield high-content screening microscopy for the four cell lines BT20, Calu_1, PLC/PRF/5 and HS695T used in this study. Measurements from high-content screening microscopy were plotted with RStudio Version 1.2.1335.

Table 1. Overview of stiffness values measured with a sharp tip (radius: 20 nm) for the cell lines BT20, Calu_1, PLC/PRF/5 and HS695T[37] and the corresponding integrated pancellular levels of tubulin and actin.

Cell line	Breast cancer (BT20)	Lung cancer (Calu_1)	Liver cancer (PLC/PRF/5)	Skin cancer (HS695T)
Pancellular level actin (a.u.)	4.64	5.00	4.06	3.70
Pancellular level tubulin (a.u.)	1.58	0.53	0.50	0.47
$E_{periphery}$ (kPa) tip radii: 20 nm	50	11	11	100–200
E_{nuclei} (kPa) tip radii: 20 nm	<10	<10	<10	100
Peak deformation (nm)	258	260	185	150

whereas unpolymerized actin or tubulin moieties abundant in the cell structure would not provide mechanical resistance. This precedence, complemented by fluorescence microscopy, advances the accuracy of cytoskeleton assessments especially in cancer studies. In conclusion, atomic force microscopy has the capacity to complement diagnostic approaches and improves the following prognosis in epithelial cancers with occult metastasis risk, based on unraveling the alterations in structural and mechanical properties in the cells at malignant to metastatic stage.

4. Experimental Section

Cell Culturing: Amelanotic melanoma cell line HS695T, liver hepatoma cell line PLC/PRF/5, and human lung cancer cell line Calu_1 were used in this study and received in the laboratory form CLS Cell Lines Service GmbH (Eppelheim, Germany). HS695T and PLC/PRF/5 were cultured at first stage in a petri flask in Dulbecco's modified Eagle's medium (DMEM) from Merck KGaA (Darmstadt, Germany) containing 10% FBS (Merck KGaA, Darmstadt, Germany) and 1% penicillin/streptomycin (Carl Roth GmbH + Co. KG, Karlsruhe Germany). Calu_1 cell line was cultured in a petri flask in 50/50 mixture of DMEM/F-12 media from ThermoFisher Scientific (Waltham, MA) containing 10% FBS and 1% penicillin/streptomycin. After ≈72 h, trypsin/EDTA (Merck) was used to detach the cells, subsequently the cells were centrifuged and seeded on plasma treated glass coverslips inside plastic petri dishes and incubated at 37 °C/5% CO_2. For reaching a large confluence of cells on coverslips, cells were fed 1–2 times before the AFM experiment, during which both samples were washed off by PBS solution (Merck) each time when changing the culture medium.

Cell Staining: Cultured melanoma, human lung cancer, and liver hepatoma cells were seeded on coverslips with 25 mm in diameter. All cancer cells used in this study were stained with TRITC-conjugated phalloidin against F-actin (Merck) and an AF-488-conjugated monoclonal antibody against β-tubulin (ThermoFisher Scientific, Waltham, MA) and counterstained with DAPI (ThermoFisher Scientific). Prior cells were fixed with 4% paraformaldehyde for 15 min and permeabilized for 10 min with 0.2% Triton in PBS. Nonspecific binding was blocked by means of 3% bovine serum albumin (BSA) in PBS, followed by 1 h of dye-loading with a ratio of 1:1000 labels diluted in 3% blocking solution.

Atomic Force Microscopy Imaging: Imaging and spectroscopy were performed as in our previous study[5] using a Bruker Icon atomic force microscope (Bruker AXS, Santa Barbara, CA) in the PeakForce tapping mode (PFT). In this mode, the cantilever was sinusoidally driven by a piezo actuator using a frequency substantially lower than the resonant frequency of the lever to limit inertial and hydrodynamic components in the sensed cantilever-tip force.[38] The tip trajectory within one oscillation cycle and a typical interaction force between tip and sample are depicted in the scheme of **Figure 10**. In case the force versus time

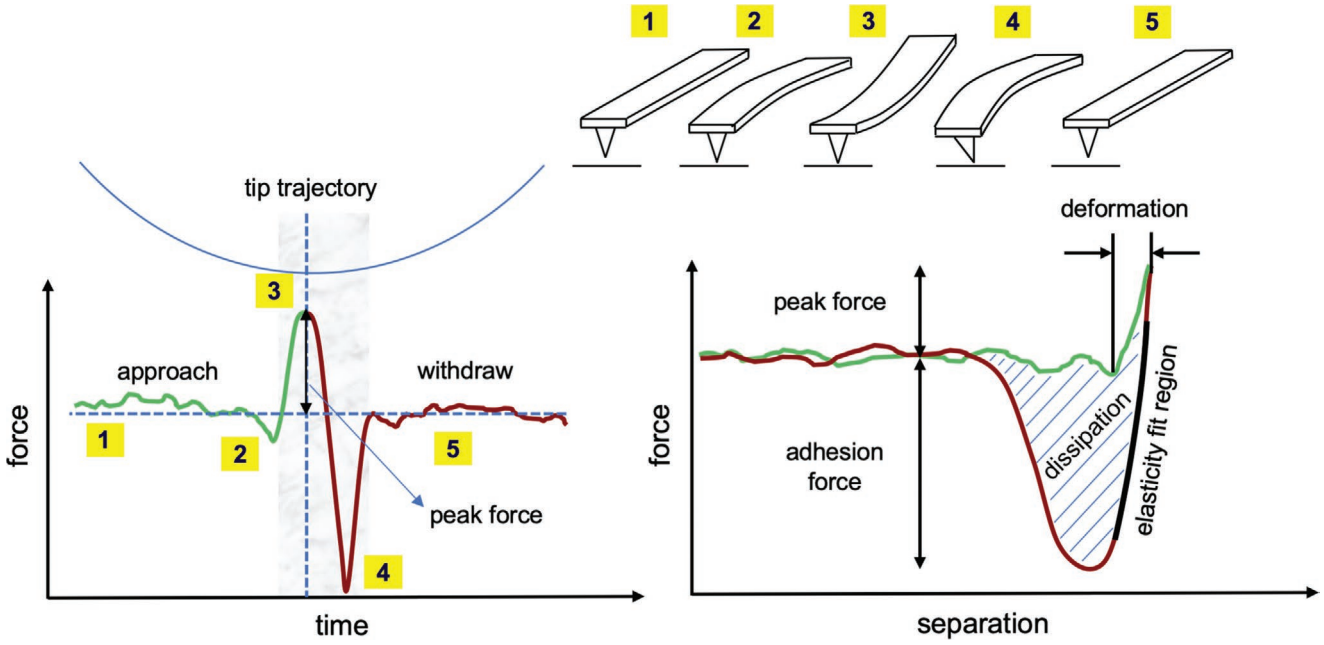

Figure 10. Scheme of a typical force versus time plot and force versus separation plot. The numbers correlate the different cantilever states with the events in the time plot. The shaded area in the force versus time plot marks the period of tip-sample contact.

cycle is synchronized with the actuator's drive voltage and the deflection sensitivity of the optical detection system as well as the cantilever's spring constant are calibrated, the force versus separation curve in each oscillation can be deduced. From this plot, the adhesion force can be read out from the force difference between the lower turning point and the zero-force line, the dissipation during one oscillation cycle from the enclosed area between approach and withdraw curve, and the sample deformation as difference between the tip-sample separation of the onset of repulsive force during approach and the separation corresponding to the maximum applied force (peak force). In addition, the force increase during approach or decrease during withdraw can be fit by an appropriate contact mechanics model. A frequently used model is the Hertz/Sneddon model that provides a relationship between the sensed force by a conical indenter and the sample deformation as follows:

$$F_{\mathrm{L}} = \frac{2}{\pi}\frac{E}{1-\upsilon^2}\tan(\alpha)\delta^2 \quad (1)$$

where F_{L} is the applied load, E is the elastic modulus of the sample, υ is the sample's Poisson ratio, α is the half opening angle of the cone and the δ indentation depth. However, due care in interpretation of the obtained data has to be taken choosing Hertz- or Sneddon-based models for extracting the elasticity of soft biological samples.[37] Cantilevers that were used had nominal force constants of 0.02 N m^{-1} (rectangular-shaped microlevers, MLCT-BIO-DC-B, nonconductive silicon nitride from Bruker) and 0.08 N m^{-1} (triangular-shaped microlevers, XNC12/CR-AU BS, nonconductive silicon nitride from MIKROMASCH, Sofia, Bulgaria) to measure gently the mechanical properties and acquire spectroscopy of the cells. To determine the exact force constant, the thermal noise method was used.[39] Typical values for the cantilever spring constant were in the range of 0.03–0.05 N m^{-1} for the MLCT-BIO-DC-B cantilevers and in the range of 0.06–0.10 N m^{-1} for the XNC12/CR-AU BS cantilevers. The deflection sensitivity was calibrated on a stiff sapphire standard sample from Bruker. Cantilever tips had pyramidal shape with a tip radius R = 20 nm and a half-opening cone angle of α = 40° for the MLCT-BIO-DC-B cantilevers and with a tip radius R = 10 nm and a half-opening cone angle of α = 35° for the XNC12/CR-AU BS cantilevers. The fundamental flexural resonant frequencies of MLCT-BIO-DC-B cantilevers in deionized water was $f_{0,\ \mathrm{flex}} \approx$ 2.0 kHz and that of XNC12/CR-AU BS cantilevers was $f_{0,\ \mathrm{flex}} \approx$ 4 kHz. The medium was changed to L-15 medium (Leibovitz) CO_2-independent (Merck) mixed with 10% FBS solution and 1% penicillin/strep when performing AFM experiments to minimize the risk of detachment or death of cells due to the change of the pH value of the culture medium. In contrast to previous study,[5] PFT-AFM was operated with a higher digital resolution of 2048 × 2048-pixel, 4096 × 4096-pixel, for ≈6 and 12 h, respectively, per images at a scan rate of 0.1 Hz for scan sizes of 93 × 93 μm^2. Consequently, the lateral resolution obtained in each image was ≈44 nm per pixel for 2048 × 2048-pixel images and 22 nm per pixel for 4096 × 4096-pixel images with even a smaller tip size. It is noted that the lateral resolution achieved on living biological cells by AFM presented in this study is unprecedented considering the overall scan size.

Fluorescence Microscopy Imaging: A Leica TCS SPE confocal point scanner mounted on a Leica DMi8 stand equipped with a 63x/1.30 ACS APO Oil CS 0.17/E,0.16 objective, a solid-state ruby laser module with 405, 488, and 561 nm excitation lasers and a Leica SP detector to acquire confocal fluorescence microscopy of cells was used. Images were analyzed using Fiji (https://imagej.net/Fiji). Cells were analyzed by high content microscopy with the Operetta automated imaging system (PerkinElmer, UK) equipped with a 20x long/0.45 NA objective, a xenon fiber optic as light source, 360–400, 460–490, and 560–580 nm excitation- and 410–480, 500–550, and 590–640 emission filters, respectively, in order to quantify integrated pancellular levels of F-actin and β-tubulin. Respective integrated pancelluar intensities were analyzed using the Harmony High-Content Imaging and Analysis Software (PerkinElmer, Akron, OH) and mean values were plotted with RStudio Version 1.2.1335.[40]

Statistical Analysis: Image processing and analysis were done with the softwares Nanoscope Analysis 1.8 (Bruker AXS, Santa Barbara, CA) and Gwyddion 2.54, respectively (Department of Nanometrology, Czech Metrology Institute, Czech Republic). Data processing and fitting of the elastic moduli and deformation values to Gaussian distribution were performed with Igor pro 6.37 (WaveMetrics, Inc, Portland, OR). For AFM study, in total five images of HS695T containing 40 cells, three images of Calu_1 containing 20 cells, four images of PLC/PRF/5 containing 24 cells were evaluated. For fluorescence analysis, 3 images on HS695T in total containing 103 cells, 3 images on Calu_1 containing 28 cells and 2 images on PLC/PRF/5 containing 50 cells were considered. Details about the image size and image resolution can be found in the atomic force microscopy imaging section.

Supporting Information

Supporting Information is available from the Wiley Online Library or from the author.

Acknowledgements

The authors thank the Deutsche Forschungsgemeinschaft (Sachbeihilfe DI 2176/2-1) for financial support. The present address for F.D.H. was corrected on July 10, 2020, after initial online publication.

Conflict of Interest

The authors declare no conflict of interest.

Keywords

carcinomas, diagnostics, fluorescence microscopy, force spectroscopy, occult metastasis

Received: February 3, 2020
Revised: May 15, 2020
Published online: June 17, 2020

[1] B. R. Gastman, P. Gerami, S. J. Kurley, R. W. Cook, S. Leachman, J. T. Vetto, *J. Am. Acad. Dermatol.* **2019**, *80*, 149.
[2] D. C. Whiteman, P. D. Baade, C. M. Olsen, *J. Invest. Dermatol.* **2015**, *135*, 1190.
[3] D. L. Morton, J. F. Thompson, A. J. Cochran, N. Mozzillo, O. E. Nieweg, D. F. Roses, H. J. Hoekstra, C. P. Karakousis, C. A. Puleo, B. J. Coventry, M. Kashani-Sabet, B. M. Smithers, E. Paul, W. G. Kraybill, J. G. McKinnon, H. J. Wang, R. Elashoff, M. B. Faries, M. Grp, *N. Engl. J. Med.* **2014**, *370*, 599.
[4] W. R. Shaikh, S. W. Dusza, M. A. Weinstock, S. A. Oliveria, A. C. Geller, A. C. Halpern, *JNCI, J. Natl. Cancer Inst.* **2016**, *108*, 7.
[5] A. Amiri, F. Hastert, L. Stühn, C. Dietz, *Nanoscale Adv.* **2019**, *1*, 4853.
[6] S. E. Cross, Y.-S. Jin, J. Rao, J. K. Gimzewski, *Nat. Nanotechnol.* **2007**, *2*, 780.
[7] A. Calzado-Martin, M. Encinar, J. Tamayo, M. Calleja, A. S. Paulo, *ACS Nano* **2016**, *10*, 3365.
[8] M. Plodinec, M. Loparic, C. A. Monnier, E. C. Obermann, R. Zanetti-Dallenbach, P. Oertle, J. T. Hyotyla, U. Aebi, M. Bentires-Alj, R. Y. H. Lim, C. A. Schoenenberger, *Nat. Nanotechnol.* **2012**, *7*, 757.

[9] T. Kwon, S. Gunasekaran, K. Eom, *Biochim. Biophys. Acta, Rev. Cancer* **2019**, *1871*, 367.
[10] A. A. Creasey, H. S. Smith, A. J. Hackett, K. Fukuyama, W. L. Epstein, S. H. Madin, *In Vitro* **1979**, *15*, 342.
[11] M. Reck, S. Popat, N. Reinmuth, D. De Ruysscher, K. M. Kerr, S. Peters, E. G. W. Grp, *Ann. Oncol.* **2014**, *25*, iii27.
[12] L. A. Byers, J. Wang, M. B. Nilsson, J. Fujimoto, P. Saintigny, J. Yordy, U. Giri, M. Peyton, Y. H. Fan, L. X. Diao, F. Masrorpour, L. Shen, W. B. Liu, B. Duchemann, P. Tumula, V. Bhardwaj, J. Welsh, S. Weber, B. S. Glisson, N. Kalhor, I. I. Wistuba, L. Girard, S. M. Lippman, G. B. Mills, K. R. Coombes, J. N. Weinstein, J. D. Minna, J. V. Heymach, *Cancer Discovery* **2012**, *2*, 798.
[13] V. S. Iglesias, L. Giuranno, L. J. Dubois, J. Theys, M. Vooijs, *Front. Oncol.* **2018**, *8*, 267.
[14] L. Ao, Y. Guo, X. Song, Q. Guan, W. Zheng, J. Zhang, H. Huang, Y. Zou, Z. Guo, X. Wang, *Liver Int.* **2017**, *37*, 1688.
[15] L. P. Waller, V. Deshpande, N. Pyrsopoulos, *World J. Hepatol.* **2015**, *7*, 2648.
[16] A. H. Hou, P. M. Voorhoeve, W. W. Lan, M. Q. Tin, L. Tong, *Exp. Cell Res.* **2013**, *319*, 2781.
[17] J. L. Gordon, M. A. Brown, M. M. Reynolds, *Diseases* **2018**, *6*, 85.
[18] R. M. Neve, K. Chin, J. Fridlyand, J. Yeh, F. L. Baehner, T. Fevr, L. Clark, N. Bayani, J.-P. Coppe, F. Tong, T. Speed, P. T. Spellman, S. DeVries, A. Lapuk, N. J. Wang, W.-L. Kuo, J. L. Stilwell, D. Pinkel, D. G. Albertson, F. M. Waldman, F. McCormick, R. B. Dickson, M. D. Johnson, M. Lippman, S. Ethier, A. Gazdar, J. W. Gray, *Cancer Cell* **2006**, *10*, 515.
[19] M. L. Sos, K. Michel, T. Zander, J. Weiss, P. Frommolt, M. Peifer, D. Li, R. Ullrich, M. Koker, F. Fischer, T. Shimamura, D. Rauh, C. Mermel, S. Fischer, I. Stuckrath, S. Heynck, R. Beroukhim, W. Lin, W. Winckler, K. Shah, T. LaFramboise, W. F. Moriarty, M. Hanna, L. Tolosi, J. Rahnenfuhrer, R. Verhaak, D. Chiang, G. Getz, M. Hellmich, J. Wolf et al., *J. Clin. Invest.* **2009**, *119*, 1727.
[20] Z. Qiu, K. Zou, L. Zhuang, J. Qin, H. Li, C. Li, Z. Zhang, X. Chen, J. Cen, Z. Meng, H. Zhang, Y. Li, L. Hui, *Sci. Rep.* **2016**, *6*, 27411.
[21] X. Deng, G. Shao, H. T. Zhang, C. Li, D. Zhang, L. Cheng, B. D. Elzey, R. Pili, T. L. Ratliff, J. Huang, C. D. Hu, *Oncogene* **2017**, *36*, 1223.
[22] G. Attard, C. Parker, R. A. Eeles, F. Schröder, S. A. Tomlins, I. Tannock, C. G. Drake, J. S. de Bono, *Lancet* **2016**, *387*, 70.
[23] T. Kobayashi, T. Masaki, E. Nozaki, M. Sugiyama, F. Nagashima, J. Furuse, H. Onishi, T. Watanabe, Y. Ohkura, *Anticancer Res.* **2015**, *35*, 6577.
[24] R. X. Yuan, Y. F. Chen, X. S. He, X. R. Wu, J. Ke, Y. F. Zou, Z. R. Cai, Y. Zeng, L. Wang, J. P. Wang, X. J. Fan, X. J. Wu, P. Lan, *J. Surg. Res.* **2013**, *183*, 163.
[25] E. S. Santos, M. Blaya, L. E. Raez, *Clin. Lung Cancer* **2009**, *10*, 168.
[26] S. Jungbauer, R. Kemkemer, H. Gruler, D. Kaufmann, J. P. Spatz, *ChemPhysChem* **2004**, *5*, 85.
[27] C. J. Wilson, R. E. Clegg, D. I. Leavesley, M. J. Pearcy, *Tissue Eng.* **2005**, *11*, 1.
[28] J. Biscan, N. Kallay, T. Smolic, *Colloids Surf., A* **2000**, *165*, 115.
[29] A. Vidyasagar, N. A. Wilson, A. Djamali, *Fibrog. Tissue Repair* **2012**, *5*.
[30] T. Miron, M. Wilchek, B. Geiger, *Eur. J. Biochem.* **1988**, *178*, 543.
[31] T. Miron, K. Vancompernolle, J. Vandekerckhove, M. Wilchek, B. Geiger, *J. Cell Biol.* **1991**, *114*, 255.
[32] Y. J. Shi, X. Y. Jiang, L. L. Zhang, H. J. Pu, X. M. Hu, W. T. Zhang, W. Cai, Y. Q. Gao, R. K. Leak, R. F. Keep, M. V. L. Bennett, J. Chen, *Proc. Natl. Acad. Sci. USA* **2017**, *114*, E1243.
[33] R. L. During, B. G. Gibson, W. Li, E. A. Bishai, G. S. Sidhu, J. Landry, F. S. Southwick, *EMBO J.* **2007**, *26*, 2240.
[34] B. W. Sheng, C. C. Qi, B. Liu, Y. Lin, T. Fu, Q. D. Zeng, *Sci. Rep.* **2017**, *7*, 13807.
[35] J. D. Konda, M. Olivero, D. Musiani, S. Lamba, M. F. Di Renzo, *Mol. Oncol.* **2017**, *11*, 599.
[36] M. Dogterom, G. H. Koenderink, *Nat. Rev. Mol. Cell Biol.* **2019**, *20*, 38.
[37] A. Amiri, F. D. Hastert, L.-O. Heim, C. Dietz, *Appl. Phys. Lett.* **2020**, *116*, 083701.
[38] C. A. Amo, R. Garcia, *ACS Nano* **2016**, *10*, 7117.
[39] H. J. Butt, M. Jaschke, *Nanotechnology* **1995**, *6*, 1.
[40] P. Zhang, A. K. Ludwig, F. D. Hastert, C. Rausch, A. Lehmkuhl, I. Hellmann, M. Smets, H. Leonhardt, M. C. Cardoso, *Nucleus* **2017**, *8*, 548.